

# **Time-resolved dynamic optical coherence tomography for retinal blood flow analysis**

Philippe Valmaggia<sup>1,2,3</sup>, Philippe C. Cattin<sup>1</sup>, Robin Sandkühler<sup>1</sup>, Nadja Inglin<sup>2</sup>,  
Tilman P. Otto<sup>4</sup>, Silke Aumann<sup>4</sup>, Michel M. Teussink<sup>4</sup>, Richard F. Spaide<sup>5</sup>,  
Hendrik P. N. Scholl<sup>2,3</sup>, Peter M. Maloca<sup>2,3</sup>

<sup>1</sup>Department of Biomedical Engineering, University of Basel, 4123 Allschwil, Switzerland

<sup>2</sup>Institute of Molecular and Clinical Ophthalmology Basel (IOB), Basel, 4031 Basel, Switzerland

<sup>3</sup>Department of Ophthalmology, University Hospital Basel, 4031 Basel, Switzerland

<sup>4</sup>Heidelberg Engineering GmbH, 69115 Heidelberg, Germany

<sup>5</sup>Vitreous Retina Macula Consultants of New York, NY 10022, USA

**Word count:** Abstract: 245; Manuscript: 4'218

**Corresponding author:** Philippe Valmaggia, Department of Biomedical Engineering, University of Basel, 4123 Allschwil, Switzerland. Email: philippe.valmaggia@unibas.ch

**Keywords:** time-resolved, dynamic, optical coherence tomography, retinal blood flow, flow velocity

**Commercial relationships:** PV received funding from the Swiss National Science Foundation (Grant 323530\_199395), the Janggen-Pöhn Stiftung and AlumniMedizin Basel and discloses personal compensation from Heidelberg Engineering GmbH. TPO, SA and MMT are salaried employees of Heidelberg Engineering GmbH, 69115 Heidelberg, Germany. RFS discloses personal compensation from Topcon Medical Systems, Roche, Bayer, Heidelberg Engineering and Genentech. HPNS is supported by the Swiss National Science Foundation (Project funding: “Developing novel outcomes for clinical trials in Stargardt disease using structure/function relationship and deep learning” #310030\_201165, and National Center of Competence in Research Molecular Systems Engineering: “NCCR MSE: Molecular Systems Engineering (phase II)” #51NF40-182895), the Wellcome Trust (PINNACLE study), and the Foundation Fighting Blindness Clinical Research Institute (ProgStar study). HPNS is a member of the Scientific Advisory Board of Boehringer Ingelheim Pharma GmbH & Co; Claris Biotherapeutics Inc.; Eluminex Biosciences; Gyroscope Therapeutics Ltd.; Janssen Research & Development, LLC (Johnson & Johnson); Novartis Pharma AG (CORE); Okuvision GmbH; ReVision Therapeutics Inc.; and Saliogen Therapeutics Inc. HPNS is a consultant of: Alnylam Pharmaceuticals Inc.; Gerson Lehrman Group Inc.; Guidepoint Global, LLC; and Intergalactic Therapeutics Inc. HPNS is member of the Data Monitoring and Safety Board/Committee of Belite Bio (CT2019-CTN-04690-1), F. Hoffmann-La Roche Ltd (VELODROME trial, NCT04657289; DIAGRID trial, NCT05126966; HUTONG trial) and member of the Steering Committee of Novo Nordisk (FOCUS trial; NCT03811561). All arrangements have been reviewed and approved by the University of Basel (Universitätsspital Basel, USB) and the Board of Directors of the Institute of Molecular and Clinical Ophthalmology Basel (IOB), in accordance with their conflict-of-interest policies. Compensation is being negotiated and administered as grants by USB, which receives them on its proper accounts. HPNS is co-director of the Institute of Molecular and Clinical Ophthalmology Basel (IOB), which is constituted as a non-profit foundation and receives funding from the University of Basel, the University Hospital Basel, Novartis and the government of Basel-Stadt. PMM is a consultant of Roche and holds intellectual properties for machine learning at MIMO AG and VisionAI, Switzerland. Funding organisations had no influence on the design, performance or evaluation of the current study. The other authors declare no conflict.

## **Abstract**

**Purpose:** Optical coherence tomography (OCT) representations in clinical practice are static and do not allow for a dynamic visualisation and quantification of blood flow. This study aims to present a method to analyse retinal blood flow dynamics using time-resolved structural optical coherence tomography (OCT).

**Methods:** We developed novel imaging protocols to acquire video-rate time-resolved OCT B-scans (1024 x 496 pixels, 10° field of view) at four different sensor integration times (integration time of 44.8  $\mu$ s at a nominal A-scan rate of 20 kHz, 22.4  $\mu$ s at 40 kHz, 11.2  $\mu$ s at 85 kHz, 7.24  $\mu$ s at 125 kHz). The vessel centres were manually annotated for each B-scan and surrounding subvolumes were extracted. We used a velocity model based on signal-to-noise ratio (SNR) drops due to fringe washout to calculate blood flow velocity profiles in vessels within five optic disc diameters of the optic disc rim.

**Results:** Time-resolved dynamic structural OCT revealed pulsatile SNR changes in the analysed vessels and allowed the calculation of potential blood flow velocities at all integration times. Fringe washout was stronger in acquisitions with longer integration times; however, the ratio of the average SNR to the peak SNR inside the vessel was similar across all integration times.

**Conclusions:** We demonstrated the feasibility of estimating blood flow profiles based on fringe washout analysis, showing pulsatile dynamics in vessels close to the optic nerve head using structural OCT. Time-resolved dynamic OCT has the potential to uncover valuable blood flow information in clinical settings.

## Introduction

Optical coherence tomography (OCT) is a technology that enables the visualisation of retinal structures on a micrometre scale.<sup>1,2</sup> Its benefits of being non-invasive, fast and easy to operate have made OCT become one of the most widely used imaging techniques, particularly in ophthalmology.<sup>3</sup> Since its first demonstration in 1991, OCT has been enhanced and nowadays, allows the visualisation of intravascular flow regions through OCT angiography (OCTA).<sup>4</sup> OCTA is based on the detection of OCT signal changes over time and allows the visualisation of chorioretinal vasculature down to the microvasculature in an unprecedented way.

However, the clinical representations of both OCT and OCTA are static. For visualising flow dynamics and analysing changes within single vessels over time, ophthalmologists and researchers must rely on other acquisition modalities such as Doppler OCT, laser speckle flowgraphy, the retinal function imager or variable interscan time analysis (VISTA) in macular OCTA.<sup>5–13</sup> These techniques are mostly used in specialised research centres and are not yet widely used in everyday clinical use. Due to the relatively high demands on technology and experience, they have not yet been implemented in a routine clinical application that can be used on a daily basis. However, the scan patterns in OCT devices are generally customisable and modifications would allow for dynamic acquisitions and visualisations in clinical settings. Sequentially acquired OCT signals at the same position particularly fluctuate within and in close proximity to vessels; accordingly, they have the greatest contribution to OCTA signal generation.<sup>4,14</sup>

The OCT signals are generated by measuring the interference pattern of reflected light waves from a sample and a reference mirror.<sup>1,15,16</sup> The reflected light waves interfere constructively or destructively, generating interference patterns of light and

101 dark bands which are called interference fringes<sup>15,17</sup> – appearing similar to the edge  
102 of a fabric fringe. When the sample or instrument moves during image acquisition,  
103 the phase of the reflected light changes. This modulation of the interference can  
104 cause the interference fringes to vanish, a phenomenon called fringe washout. The  
105 fringe washout leads to a signal-to-noise ratio (SNR) drop in the image, which tends  
106 to be larger in case of a larger sample motion.<sup>18–20</sup> This can occur at higher sample  
107 velocities or increased sensor integration times.<sup>18</sup> Taking advantage of the  
108 knowledge that fringe washout is directly linked to the velocity of the sample motion,  
109 we investigated the possibility of calculating flow profiles in time-resolved structural  
110 OCT data. An overview of the general principle of fringe washout can be found in  
111 Figure 1.

112 To investigate blood flow velocity, we modified the OCT scan patterns of a  
113 commercially available device to allow for time-resolved dynamic acquisitions.  
114 Furthermore, we analysed these images regarding the fringe washout and present  
115 dynamically calculated blood flow profiles.

## Methods

### Data acquisition

Data were acquired at the Augenarztpraxis Dr. Maloca in Lucerne, Switzerland. The study was performed according to the Declaration of Helsinki, and ethics approval was granted by the Ethics Committee of Northwestern and Central Switzerland (EKNZ 2021-02360). Written informed consent was obtained from all participants.

The images were acquired with a Heidelberg Spectralis OCT with an investigational acquisition module. The OCT volume acquisition pattern was modified to continuous B-scans with a 10° field of view without OCT tracking through the on-board dual-beam confocal scanning laser ophthalmoscope tracking system. This prevented irregular OCT B-scan acquisition due to compensatory OCT-beam steering by the tracking system, which has a variable time lag. The patients were informed about the acquisition procedure to ensure good image quality. The subjects were instructed to fixate on the foveal fixation target, close their eyes, blink once and then leave their eyes open. Acquisitions were performed for several seconds, where a manual press on the joystick of the OCT device allowed to start and end the acquisition. In the case of blinks or major ocular movements, the process was repeated.

The acquisitions were performed between the optic nerve head centre and five optic disc diameters (ODDs) from the optic nerve rim and graded by eccentricity 0–6 (0: optic nerve head centre, 1: neuroretinal rim, 2: 1 ODD superotemporal to the neuroretinal rim, 3: 2 ODDs, 4: 3 ODDs, 5: 4 ODDs, 6: 5 ODDs). The major visible vessels were imaged perpendicularly, so that the cross-section was visible.

All time-resolved acquisitions were performed with continuous B-scans, each single scan comprising 1024 A-scans with 496 pixels, with a 10° field of view. This allowed

the same B-scan to be repeated at the same location with a high sampling density over a longer period of time and still meet the requirements regarding light safety. All locations were acquired at four different A-scan integration times 44.8, 22.4, 11.2 and 7.24  $\mu$ s, corresponding to nominal A-scan rates of 20, 40, 85 and 125 kHz, respectively. This enabled video-rate sequential B-scan acquisitions. Each separate B-scan was saved as a single image without averaging. Notably, the SNR in spectral-domain (SD) OCTs depends on the integration time according to the following established formula<sup>21–23</sup>:

$$SNR_{SD} \sim (\eta * P_{sample} * \tau_i) / E_v,$$

where  $\eta$  corresponds to the spectrometer efficiency,  $P_{sample}$  to the power returned in the sample arm,  $\tau_i$  to the integration time and  $E_v$  to the energy per photon. A validation of this formula was investigated during this in vivo study. The SNR for each individual B-scan was calculated with the raw data by the ratio of the maximum intensity to the noise level. Overall, the SNR values were compared for each integration time.

## **Image processing**

All image stacks were exported from the OCT device in normalised raw format (.vol files, image intensities normalised between 0 and 1 at a B-scan level). In the first step, all image stacks were transformed for a visual representation by multiplying all image intensities by 255 times the 4<sup>th</sup> square root of the normalised intensity. These transformed images stacks were then registered using a rigid body transformation model with a pyramid processing scheme.<sup>24</sup> This registration pipeline was adapted to reduce the effect of speckle noise in the registration process. The mean of the first 10 images of the image stack was used as the reference image for the registration of

the complete image stack. Rigid body registration was applied to prevent distortion of the retina and to allow visualisation of the time-resolved B-scan stack. In the second step, the vessel centres of prominently visible vessels were manually annotated, and subvolumes of  $7 \times 7$  pixels around the centre were extracted from each B-scan. This subvolume corresponded to physical dimensions of  $20 \mu\text{m}$  along the B-scan axis and  $27 \mu\text{m}$  along the A-scan axis.

In a second step, the extracted subvolumes were analysed with their original, non-normalised intensities, which were obtained from the metadata of the .vol files. The SNR in the individual vessel subvolumes were then calculated as the ratio of the average pixel intensity in the subvolume to the noise level of the B-scan, assuming shot noise limited detection. The noise level of the B-scan was approximated using the Heidelberg Quality score (in dB) and the maximum intensity value of the B-Scan. A depth-specific noise level to account for roll-off was not obtainable with the present data. An overview of the main image processing steps is shown in Figure 2.

### **Flow profile generation**

Fringe washout is a phenomenon occurring when imaged particles are moving which leads to a SNR drop in the OCT image. The effect is linked to the integration time and is attributed to the modulation of the interference signal when particles are in motion. Typically, the fringe washout is more pronounced as the integration time increases. Yun et al. presented formulas for the fringe washout describing separately the axial and lateral components of particle movements.<sup>18</sup> In the case of oblique motion, the axial component is orders of magnitude larger when compared with the lateral component.<sup>19</sup> In this work, we used the squared sinc function presented for the axial component of the fringe washout to calculate blood flow velocity profiles<sup>18</sup>:

188  $SNR_{Drop} = \sin(k_0 \Delta z)^2 / (k_0 \Delta z)^2,$

189 where  $k_0 = 2\pi / \lambda$  and  $\Delta z = n \cdot v \cdot \tau$ .  $k_0$  corresponds to the central wavenumber of  
190 the light source,  $\lambda$  to the central wavelength of the light source,  $\Delta z$  to the  
191 displacement in the z-axis,  $n$  to the refractive index of the eye,  $\tau$  to the integration  
192 time, and  $v$  to the velocity.

193 This quadratic sinc function, with a known SNR drop, was solved numerically for  
194 velocity. All numerical solutions per B-scan were stored as a potential flow velocity.  
195 The results of the equation for each B-scan,  $SNR_{Drop}$ , were used to generate the  
196 dynamic flow profiles. Figure 3 presents the  $SNR_{Drop}$  profiles at the four acquisition  
197 rates with calculated velocities in mm/s for any moving object. For this study, the  
198 average SNR of the  $7 \times 7$  B-scan subvolume was divided by the maximum SNR at  
199 the pixel level of the complete vessel subvolume ( $7 \times 7 \times$  number of B-scans) to  
200 calculate the  $SNR_{Drop}$ . All calculations were made with absolute SNR values. The  
201 calculated velocities are presented in arbitrary units since the formula only takes into  
202 account the axial component and the SNR inside the vessels without flow, which  
203 would be the reference for  $SNR_{Drop}$  calculations, could not be determined.

## 204 **Data analysis**

205 The generated flow profiles were quantitatively and qualitatively analysed. On a  
206 qualitative level, the generated dynamic OCTs and the course of the pulse waves  
207 were analysed. The quantitative analysis was focused on the flow profiles, where the  
208 minimal, maximal, and average velocities for each vessel at each B-scan were  
209 calculated. The minimal velocity refers to the smallest numerical solution of the  
210  $SNR_{Drop}$  equation, the maximum velocity refers to the largest solution, and the  
211 average velocity refers to the average of all numerical solutions per B-scan.

212 Furthermore, the exam duration, the SNR of the B-scans, the mean and maximal  
213 intensity of the subvolumes, and the maximum image intensity in the raw data were  
214 analysed. Programming was performed with Linux shell scripts, Python 3.9 (Python  
215 Software Foundation, Wilmington, USA) and R V4.2.2 (Foundation for Statistical  
216 Computing, Vienna, Austria). The data were visualised with Python 3.9, R V4.2.2  
217 and 3DSlicer V4.11.<sup>25,26</sup>

## Results

A total of 164 time-resolved image stacks from six healthy subjects were acquired and manually annotated. All acquisitions were performed in the right eyes of the patients. The image stacks consisted of 47 to 483 B-scans, and between 1 and 5 vessels were annotated per volume. In summary, 466 vessels were annotated in the time-series data, totalling 94,619 annotated vessel centres.

### Qualitative analysis

Time-resolved dynamic acquisitions of structural OCT are feasible in healthy subjects and show changes in reconstructed images over time. These changes are of different nature, where pulsatile profiles can be clearly identified. Supplementary Video 1 shows the pulsation inside an artery at the centre of the optic nerve as changes in image intensity. Furthermore, we can see pulsation of the optic nerve head tissue. Supplementary Video 2 shows a longitudinal cut through the same artery, where we can observe the fringe washout along the vessel. We detected an increase in the fringe washout at the centre of the vessel, showing a higher relative flow velocity. In addition, we identified a bimodal peak of the fringe washout.

Qualitative analysis of the generated flow profiles confirmed this pulsatility for the SNR changes and the calculated flow velocities. As depicted for an acquisition at the optic nerve head centre in Figure 4, the flow profiles show pulsatility where maximal and minimal velocities were clearly distinguishable. In addition, the flow velocities showed a rapid increase, followed by a gradual decrease towards a steady-state until the pulsatile cycle restarted. As shown in Figure 5, this flow profile could be visualised at all four acquisition rates, with a constant repetition of approximately four pulse visualisations within 3 s. These observations suggest that the pulsation

propagates in correspondence with the cardiac cycle, which corresponds in this example to a heart rate of 80 beats per minute.

When analysing the blood flow profiles at different eccentricities, pulsatility was evident close to the optic nerve centre. The pulsatility decreased towards the periphery, where a distinct change tended to occur when the vessel crossed the optic nerve head rim. Figure 6 provides a visual representation of this finding by showing the calculated blood flow profiles along with an en-face representation of their acquisition location. Further, we observed a decrease of the estimated average flow velocity towards the periphery, here again with an apparent decrease at the crossing of the vessel of the optic nerve head rim.

## **Quantitative analysis**

We validated whether the SNR variability inside the vessels was different from the SNR variability in adjacent tissue, as the fringe washout variability could occur due to axial bulk motion. For this analysis, we annotated further retinal nerve fibre layer (RNFL) subvolumes in the proximity of an artery as the RNFL is known to have a high reflectivity in OCT.<sup>27</sup> We analysed the SNR in the vessel ( $\text{SNR}_{\text{vessel}}$ ), the SNR in the RNFL ( $\text{SNR}_{\text{RNFL}}$ ) and the SNR in the complete B-scan ( $\text{SNR}_{\text{B-scan}}$ ). The analysis confirmed that the  $\text{SNR}_{\text{vessel}}$  was lower than the  $\text{SNR}_{\text{RNFL}}$ . The  $\text{SNR}_{\text{B-scan}}$  was the highest as it was defined by the peak SNR in the complete image. The  $\text{SNR}_{\text{vessel}} / \text{SNR}_{\text{B-scan}}$  ratio vessel clearly decreased with longer integration times while the  $\text{SNR}_{\text{RNFL}} / \text{SNR}_{\text{B-scan}}$  ratio showed less variability. This showed that the fringe washout inside the vessels was stronger at longer integration times. The SNR comparison of the artery and the RNFL are further described for the different integration times in Table 1. A visualisation of the fringe washout at the different

266 integration times can be found in the Supplementary Video 3, where the SNR drops  
267 diminish with faster acquisitions.

268 An overview of the statistics and the calculated velocities per A-scan rate can be  
269 found in Tables 2 and 3. When analysing the absolute SNRs,  $SNR_{B-scan}$  and  
270  $SNR_{Vessel}$  correlated with integration time. The calculated factors of the integration  
271 times of 44.8  $\mu s$  at a nominal A-scan rate of 20 kHz, 22.4  $\mu s$  at 40 kHz 11.2  $\mu s$  at 85  
272 kHz, 7.24  $\mu s$  at 125 kHz are 6.19, 3.09, and 1.55 to 1 when taking the shortest  
273 integration time as a reference. Median  $SNR_{B-scan}$  factors are 5.83, 3.73, and 1.75 to  
274 1, respectively. In summary, a longer integration time led to an increase of both  
275 absolute  $SNR_{Vessel}$  and  $SNR_{B-scan}$ , and a decrease of the  $SNR_{Vessel} / SNR_{B-scan}$  ratio.  
276 This is also shown in the  $SNR_{Subvolume} / SNR_{B-scan}$  for the arteries in Table 1.

277 The  $SNR_{Vessel} / \text{Peak } SNR_{Vessel}$  ratio corresponds to the SNR drop with which the flow  
278 velocities were calculated. This ratio remained constant across the varying  
279 integration times. Given that Yun et al.'s model for flow velocities is dependent on  
280 the integration time, the calculated flow velocities showed a linear relationship with  
281 their integration time ratio.<sup>18</sup> In the analysis of the flow velocities at different  
282 distances from the optic nerve head of the complete cohort, decreasing calculated  
283 mean flow velocity along the vessel arch were observed. A summary overview of the  
284 flow velocities along the vessel arch is shown in Figure 7, with corresponding  
285 examples of SLOs.

## Discussion

To analyse the dynamics within retinal structures and, more specifically, in vessels, we developed acquisition protocols for dynamic time-resolved OCT measurements utilising a commercially available OCT device widely used in clinics. Taking advantage of the fringe washout phenomenon of spectral-domain OCTs, we calculated time-resolved velocity profiles based on the SNR drop within the vessels. In addition, we found pulsatile blood flow profiles, where the amplitude and average velocity decreased from the centre of the optic nerve head towards the retinal periphery.

This study presents several novel possibilities for the analysis of OCT data acquired with a commercially available device. First, time-resolved dynamic OCT with a matching of B-scans to a time axis allowed us to assess structural changes with an interval of as low as 9 ms between B-scans. The matching of the B-scans to a time axis allowed for generating videos with real interframe intervals (Supplementary Videos 1 and 2). Considering that inter-B-scan intervals differ when tracking is activated and individual B-scans are averaged, continuous visualisations of B-scans can create an incorrect impression of the speed at which changes happen.

Second, this study presents methods for comparing OCT acquisitions with different integration times. As OCT phenomena, such as the fringe washout, are affected by the integration time, it is important to consider parameters such as the image quality or the OCT intensity, which vary with different integration times.<sup>18,28</sup> In this study, we showed in vivo that the fringe washout phenomenon varies for different integration times. The fringe washout in vessels was stronger at longer integration times, which should be considered in further studies.

310 Third, we combined this knowledge to investigate and visualise pulsatile dynamics  
311 within vessels in structural OCT. For this, we took advantage of the fact that the  
312 fringe washout analysis allows for the calculation of corresponding flow velocities.  
313 We generated blood flow profiles by calculating the flow velocity of the axial motion  
314 component for each time-resolved B-scan. OCT is primarily utilised for visualising  
315 retinal tissue, but it provides several advantages over OCTA in certain scenarios. In  
316 particular, structural OCT allows to directly work with the raw intensities from the  
317 acquisition as opposed to post-processed images. As a result, OCT can also be  
318 advantageous for the analysis of vessels, as it provides direct information about the  
319 characteristics of the tissue being imaged.

320 The analysis of the fringe washout would generally allow the calculation of velocities  
321 in mm/s. However, there are several limitations to quantitative values that we could  
322 not address in this work. The fringe washout is composed of axial and lateral  
323 components. Weighing both components is possible if the angle of the vessel and  
324 sample motion is known.<sup>29</sup> However, the axial component is larger by orders of  
325 magnitude compared with the lateral component in the case of oblique motion.<sup>19</sup> A  
326 further limitation that must be addressed is the reference intensity to calculate the  
327 SNR drop, which cannot be determined in a moving system. The optical properties of  
328 the eye, such as the clarity of the optical media as the lens, the cornea or even the  
329 momentaneous tear film affect the SNR.<sup>30</sup> Furthermore, the peak SNR inside a  
330 vessel is also affected by fringe washout, as there is permanent motion in a larger  
331 vessel in vivo. Hence, an absolute reference value or an external calibration seems  
332 difficult to determine, even under ideal circumstances. Further, the sensitivity roll-off  
333 along the A-scan axis was not assessed and hence not included in the noise  
334 calculations. An analysis of the transformation matrices used in the registration

process could assist in calculating the fringe washout component caused by bulk eye motion. In this work, we focused on the analysis of the axial component of the fringe washout to calculate potential blood flow velocities and estimate relative flow profiles in vivo. For this, we calculated numerical solutions to the  $SNR_{Drop}$  equation representing potential axial flow velocities. We present estimated flow velocity profiles in arbitrary units as an average of all the numerical solutions per B-Scan. It's important to note that these velocity profiles are estimates as there are multiple numerical solutions to the  $SNR_{Drop}$  equation. Potentially, for certain B-scans a lower numerical solution could represent the real velocity, while for others with the same  $SNR_{Drop}$  a higher numerical solution would be correct. To determine which numerical solutions to the equation accurately reflect the true axial flow velocity values, further validation of the technique is required.

An objective reference value could help align the different flow velocities we found at different acquisition rates by using the formula by Yun et al.<sup>18</sup> The calculated average, minimum and maximum flow velocities seem to be inversely dependent on the integration time as shown in Table 3. Further, we found that the absolute SNR in the vessels increases with increasing integration time, however, that the relative SNR drop within the vessels remained constant across the integration times. The major advantage of this finding is that blood flow profiles can be estimated and visualised independently from the integration time, even at higher acquisition rates where there is less relative fringe washout.

The decreasing velocity of the flow profiles along the vessel arch suggest that the method can grasp decreasing velocities in accordance with known physiologic principles. However, this cannot yet be supported by our data as the angle between the beam and the flow direction varies across the retina. Such changes in the angle

also affect the axial velocity component. In accordance with this, we noticed that the pulsatility of the calculated blood flow profiles tends to decrease when an artery crosses the optic nerve head rim. For a precise measurement of the flow velocity, again the lateral component or the angle of the vessel would have to be known.<sup>29</sup> Other techniques to measure retinal blood flow exist, such as Doppler OCT, laser speckle flowgraphy and VISTA in OCTA.<sup>5,6,8,31</sup> The analysis of retinal blood flow based on intensity changes has also been presented for a neural network-based approach.<sup>32</sup> However, these technologies are mainly used in research environments and are not yet regularly in clinical practice as the required phase information or A-scan acquisition rates are not widely available. Our method allows to calculate retinal blood flow velocity profiles with a widely used clinical device while at the same time contributing to bridge the gap left by other measurement techniques. Techniques such as laser Doppler flowmetry can only be used if the Doppler angle is known; laser speckle flowgraphy does not allow for a depth-resolved flow measurement; and VISTA is an extension of OCTA that has been presented for the macular area only.<sup>8,31</sup> This could be mainly due to the fact that the line rates of the lasers are currently not high enough to measure changes in the saturation of signal changes for VISTA outside the macular area. With further validation, our method could allow the visualisation of depth- and time-resolved flow profiles, as shown in this study for vessels around the optic nerve head. Ideally, our method could be further enhanced by including Doppler angle and phase shift information to translate combined findings into clinical practice.<sup>5,10,19</sup> A validation of newly obtained blood flow profile values could be achieved by comparing them with measurements from flow phantoms.<sup>19</sup>

384 To analyse retinal blood flow is relevant as the vasculature is involved in many  
385 ocular diseases, such as diabetic retinopathy and glaucoma. Blood flow  
386 disturbances, such as haemorrhage or ischemic attacks, can lead to vision loss and  
387 identifying vessels at risk could help prevent vascular injuries. For accurate and  
388 easy-to-use measurements, blood flow measurements must be implemented in  
389 clinics. We aim to contribute to this goal with the proposed time-resolved structural  
390 OCT-generated flow profiles. Thus far, our method has only been tested in healthy  
391 participants and not yet in subjects with ocular diseases. The short-term  
392 reproducibility for the generation of flow profiles at the same location was good. Very  
393 similar flow profiles could be generated during acquisitions with different integration  
394 times at the same location. Short-term reproducibility at the same location with the  
395 same integration time as well as inter-visit reproducibility and variability still need to  
396 be determined. The method could be further validated by imaging subjects with  
397 diseases such as glaucoma or diabetic retinopathy, as their blood flow has been  
398 shown to be altered with other measuring techniques.<sup>33–35</sup> The new estimates of  
399 retinal blood flow profiles could also be compared against the previously described  
400 techniques in further studies.

401 Future work will include a deeper analysis of the pulsatile flow profiles. As shown in  
402 Figures 4 and 5 and Supplementary Videos 2 and 3, the pulse wave appeared to  
403 have a bimodal peak, which would be congruent with the propagation of the aortic  
404 pulse wave.<sup>36</sup> In addition, the pulse wave analysis, in combination with absolute  
405 velocity and flow information, could also be used to analyse the retinal blood flow  
406 volume and parts of the cardiac output arriving at the eye from the heart.<sup>10,37</sup> An  
407 extension of this could also include the investigation of the best acquisition location,  
408 differences across branching points and general differences between arteries and

veins. The current measurements are consecutive B-scan acquisitions over time, with a minimal inter-B-scan interval of ~9 ms at 1024 A-scans. With fast acquisition speeds and a small number of B-scans, 4D cross-sectional acquisitions can become feasible. Hereby, the pulsatile nature of the fringe washout indicates a correlation with the cardiac cycle and a representation of the pulse propagation in the vasculature of the optic nerve head. In vivo measurements could investigate the validity of models about the pulse propagation towards the eye.<sup>38</sup>

## Conclusions

In summary, this study showed that time-resolved OCT acquisitions are feasible in vivo and that continuous acquisitions over several seconds can be made with a widely used clinical device. We showed that dynamic blood flow profiles can be calculated from time-resolved OCT acquisitions. Time-resolved dynamic OCT, with its high spatial and temporal resolution, holds promising information that can be further investigated as a novel clinically applicable parameter for the assessment of retinal blood flow velocity profiles.

## Acknowledgements

The authors wish to thank the Swiss National Science Foundation, the Janggen-Pöhn-Stiftung and the AlumniMedizin Basel for their financial support of this project. In addition, the researchers would like to thank all the participants who volunteered for this study.

## 431   **References**

- 432   1.     Huang D, Swanson EA, Lin CP, Schuman JS, Stinson WG, Chang W, Hee MR, Flotte  
433         T, Gregory K, Puliafito CA, Fujimoto JG. Optical coherence tomography. *Science*.  
434         1991;254(5035):1178-1181. doi:10.1126/science.1957169
- 435   2.     Chinn SR, Swanson EA, Fujimoto JG. Optical coherence tomography using a  
436         frequency-tunable optical source. *Opt Lett*. 1997;22(5):340. doi:10.1364/ol.22.000340
- 437   3.     Fujimoto J, Swanson E. The development, commercialization, and impact of optical  
438         coherence tomography. *Investig Ophthalmol Vis Sci*. 2016;57(9):OCT1-OCT13.  
439         doi:10.1167/iovs.16-19963
- 440   4.     Spaide RF, Fujimoto JG, Waheed NK, Sadda SR, Staurengi G. Optical coherence  
441         tomography angiography. *Prog Retin Eye Res*. 2018;64:1-55.  
442         doi:10.1016/j.preteyeres.2017.11.003
- 443   5.     Leitgeb RA, Werkmeister RM, Blatter C, Schmetterer L. Doppler Optical Coherence  
444         Tomography. *Prog Retin Eye Res*. 2014;41:26-43.  
445         doi:10.1016/j.preteyeres.2014.03.004
- 446   6.     Sugiyama T. Basic technology and clinical applications of the updated model of laser  
447         speckle flowgraphy to ocular diseases. *Photonics*. 2014;1(3):220-234.  
448         doi:10.3390/photonics1030220
- 449   7.     Wang L, Jiang H, Grinvald A, Jayadev C, Wang J. A Mini Review of Clinical and  
450         Research Applications of the Retinal Function Imager. *Curr Eye Res*. 2018;43(3):273-  
451         288. doi:10.1080/02713683.2017.1414853
- 452   8.     Ploner SB, Moulton EM, Choi W, Waheed NK, Lee B, Novais EA, Cole ED, Potsaid B,  
453         Husvot L, Schottenhamml J, Maier A, Rosenfeld PJ, Duker JS, Hornegger J,  
454         Fujimoto JG. Toward quantitative optical coherence tomography angiography:  
455         Visualizing blood flow speeds in ocular: Pathology using variable interscan time  
456         analysis. In: *Retina*. Vol 36. NIH Public Access; 2016:S118-S126.  
457         doi:10.1097/IAE.0000000000001328
- 458   9.     White BR, Nassif N, Boer JF de, Cense B, Bouma BE, Park BH, Chen TC, Tearney  
459         GJ, Pierce MC. In vivo dynamic human retinal blood flow imaging using ultra-high-  
460         speed spectral domain optical Doppler tomography. *Opt Express*, Vol 11, Issue 25, pp  
461         3490-3497. 2003;11(25):3490-3497. doi:10.1364/OE.11.003490
- 462   10.    Baumann B, Potsaid B, Kraus MF, Liu JJ, Huang D, Hornegger J, Cable AE, Duker  
463         JS, Fujimoto JG, Flammer J, Orgül S, Costa VP, Orzalesi N, Kriegelstein GK, Serra  
464         LM, Renard JP, Stefánsson E, Huang D, Swanson EA, Lin CP, Schuman JS, Stinson  
465         WG, Chang W, Hee MR, Flotte T, Gregory K, Puliafito CA, Fujimoto JG. Total retinal  
466         blood flow measurement with ultrahigh speed swept source/Fourier domain OCT.  
467         *Biomed Opt Express*, Vol 2, Issue 6, pp 1539-1552. 2011;2(6):1539-1552.  
468         doi:10.1364/BOE.2.001539
- 469   11.    Werkmeister RM, Dragostinoff N, Palkovits S, Told R, Boltz A, Leitgeb RA, Gröschl M,  
470         Garhöfer G, Schmetterer L. Measurement of Absolute Blood Flow Velocity and Blood  
471         Flow in the Human Retina by Dual-Beam Bidirectional Doppler Fourier-Domain  
472         Optical Coherence Tomography. *Invest Ophthalmol Vis Sci*. 2012;53(10):6062-6071.  
473         doi:10.1167/IOVS.12-9514
- 474   12.    Wartak A, Beer F, Desissaire S, Baumann B, Pircher M, Hitzenberger CK.  
475         Investigating spontaneous retinal venous pulsation using Doppler optical coherence  
476         tomography. *Sci Reports* 2019 91. 2019;9(1):1-11. doi:10.1038/s41598-019-40961-4

- 477 13. Arya M, Rashad R, Sorour O, Moulton EM, Fujimoto JG, Waheed NK. Optical  
478 Coherence Tomography Angiography (OCTA) Flow Speed Mapping Technology for  
479 Retinal Diseases. *Expert Rev Med Devices*. 2018;15(12):875.  
480 doi:10.1080/17434440.2018.1548932
- 481 14. Maloca PM, Feu-Basilio S, Schottenhamml J, Valmaggia P, Scholl HPN, Rosinés-  
482 Fonoll J, Marin-Martinez S, Inglin N, Reich M, Lange C, Egan C, Zweifel S, Tufail A,  
483 Spaide RF, Zarranz-Ventura J. Reference database of total retinal vessel surface  
484 area derived from volume-rendered optical coherence tomography angiography. *Sci*  
485 *Rep*. 2022;12(1). doi:10.1038/s41598-022-07439-2
- 486 15. Schmitt JM. Optical Coherence Tomography (OCT): a review. *IEEE J Sel Top*  
487 *Quantum Electron*. 1999;5(4):1205-1215. doi:10.1109/2944.796348
- 488 16. Aumann S, Donner S, Fischer J, Müller F. Optical Coherence Tomography (OCT):  
489 Principle and Technical Realization. In: *High Resolution Imaging in Microscopy and*  
490 *Ophthalmology*. Springer; 2019:59-85. doi:10.1007/978-3-030-16638-0\_3
- 491 17. Yaqoob Z, Wu J, Yang C. Spectral domain optical coherence tomography: a better  
492 OCT imaging strategy. *Biotechniques*. 2005;39(6 Suppl). doi:10.2144/000112090
- 493 18. Yun SH, Tearney GJ, de Boer JF, Bouma BE. Motion artifacts in optical coherence  
494 tomography with frequency-domain ranging. *Opt Express*. 2004;12(13):2977.  
495 doi:10.1364/opex.12.002977
- 496 19. Walther J, Mueller G, Morawietz H, Koch E. Signal power decrease due to fringe  
497 washout as an extension of the limited Doppler flow measurement range in spectral  
498 domain optical coherence tomography. *J Biomed Opt*. 2010;15(4):041511.  
499 doi:10.1117/1.3466578
- 500 20. Szkulmowski M, Wojtkowski M, Huang D, Swanson EA, Lin CP, Schuman JS, Stinson  
501 WG, Chang W, Hee MR, Flotte T, Gregory K, Puliafito CA, Fujimoto JG, Szkulmowski  
502 M, Gorczynska I, Bukowska D, Wojtkowski M, Targowski P. Averaging techniques for  
503 OCT imaging. *Opt Express, Vol 21, Issue 8, pp 9757-9773*. 2013;21(8):9757-9773.  
504 doi:10.1364/OE.21.009757
- 505 21. Spaide RF, Valmaggia P, Maloca PM, Scholl HPN, Otto TP, Caujolle S. Imaging the  
506 vitreous with a novel boosted optical coherence tomography technique: Vitreous  
507 degeneration and cisterns. *Retina*. 2022;42(8):1433-1441.  
508 doi:10.1097/IAE.0000000000003474
- 509 22. De Boer JF, Leitgeb R, Wojtkowski M, Huang D, Swanson EA, Lin CP, Schuman JS,  
510 Stinson WG, Chang W, Hee MR, Flotte T, Gregory K, Puliafito CA, Fujimoto JG.  
511 Twenty-five years of optical coherence tomography: the paradigm shift in sensitivity  
512 and speed provided by Fourier domain OCT [Invited]. *Biomed Opt Express, Vol 8,*  
513 *Issue 7, pp 3248-3280*. 2017;8(7):3248-3280. doi:10.1364/BOE.8.003248
- 514 23. Choma MA, Sarunic M V., Izatt JA, Yang C. Sensitivity advantage of swept source  
515 and Fourier domain optical coherence tomography. *Opt Express, Vol 11, Issue 18, pp*  
516 *2183-2189*. 2003;11(18):2183-2189. doi:10.1364/OE.11.002183
- 517 24. Thévenaz P, Ruttimann UE, Unser M. A pyramid approach to subpixel registration  
518 based on intensity. *IEEE Trans Image Process*. 1998;7(1):27-41.  
519 doi:10.1109/83.650848
- 520 25. Sjöberg DD, Whiting K, Curry M, Lavery JA, Larmarange J. Reproducible Summary  
521 Tables with the gtsummary Package. *R J*. 2021;13(1):570-580. doi:10.32614/rj-2021-  
522 053

26. Fedorov A, Beichel R, Kalpathy-Cramer J, Finet J, Fillion-Robin JC, Pujol S, Bauer C, Jennings D, Fennessy F, Sonka M, Buatti J, Aylward S, Miller J V., Pieper S, Kikinis R. 3D Slicer as an image computing platform for the Quantitative Imaging Network. *Magn Reson Imaging*. 2012;30(9):1323-1341. doi:10.1016/j.mri.2012.05.001
27. Jørgensen TM, Thomadsen J, Christensen U, Soliman W, Sander B. Enhancing the signal-to-noise ratio in ophthalmic optical coherence tomography by image registration—method and clinical examples. *J Biomed Opt*. 2007;12(4):041208. doi:10.1117/1.2772879
28. Spaide RF, Valmaggia P, Maloca PM. IMAGING the VITREOUS with A NOVEL BOOSTED OPTICAL COHERENCE TOMOGRAPHY TECHNIQUE: Posterior Vitreous Detachment. *Retina*. 2022;42(8):1425-1432. doi:10.1097/IAE.0000000000003500
29. Walther J, Koch E. Flow measurement by using the signal decrease of moving scatterers in spatially encoded Fourier domain optical coherence tomography. In: *Optical Coherence Tomography and Coherence Domain Optical Methods in Biomedicine XIII*. Vol 7168. SPIE; 2009:71681S. doi:10.1117/12.808737
30. Van Velthoven MEJ, Van Der Linden MH, De Smet MD, Faber DJ. Influence of cataract on optical coherence tomography image quality and retinal thickness. *Br J Ophthalmol*. 2006;90:1259-1262. doi:10.1136/bjo.2004.097022
31. Choi W, Moulton EM, Waheed NK, Adhi M, Lee B, Lu CD, De Carlo TE, Jayaraman V, Rosenfeld PJ, Duker JS, Fujimoto JG. Ultrahigh Speed Swept Source OCT Angiography in Non-Exudative Age-Related Macular Degeneration with Geographic Atrophy. *Ophthalmology*. 2015;122(12):2532. doi:10.1016/J.OPHTHA.2015.08.029
32. Braaf B, Donner S, Uribe-Patarroyo N, Bouma BE, Vakoc BJ. A Neural Network Approach to Quantify Blood Flow from Retinal OCT Intensity Time-Series Measurements. *Sci Rep*. 2020;10(1). doi:10.1038/s41598-020-66158-8
33. Grieshaber MC, Flammer J. Blood flow in glaucoma. *Curr Opin Ophthalmol*. 2005;16(2):79-83. doi:10.1097/01.icu.0000156134.38495.0b
34. Flammer J, Orgül S, Costa VP, Orzalesi N, Kriegelstein GK, Serra LM, Renard JP, Stefánsson E. The impact of ocular blood flow in glaucoma. *Prog Retin Eye Res*. 2002;21(4):359-393. doi:10.1016/S1350-9462(02)00008-3
35. Schmetterer L, Wolzt M. Ocular blood flow and associated functional deviations in diabetic retinopathy. *Diabetologia*. 1999;42(4):387-405. doi:10.1007/s001250051171
36. Gurovich AN, Braith RW. Pulse wave analysis and pulse wave velocity techniques: Are they ready for the clinic. *Hypertens Res*. 2011;34(2):166-169. doi:10.1038/hr.2010.217
37. Levy JH, Kouz K, Scheeren TWL, De Backer D, Saugel B. ClinicaL FoCUS Review Pulse Wave Analysis to Estimate Cardiac Output. *Anesthesiology*. 2021;134:119-145. doi:10.1097/ALN.0000000000003553
38. Jin Y, Wang X, Irnadiastputri SFR, Mohan RE, Aung T, Perera SA, Boote C, Jonas JB, Schmetterer L, Girard MJA. Effect of changing heart rate on the ocular pulse and dynamic biomechanical behavior of the optic nerve head. *Investig Ophthalmol Vis Sci*. 2020;61(4):27-27. doi:10.1167/iovs.61.4.27

569 **Table 1.** Vessel–RNFL comparison of SNR

570

Variable	20 kHz, N = 78	40 kHz, N = 132	85 kHz, N = 228	125 kHz, N = 351
<b>SNR<sub>B-scan</sub> [dB]</b>	39.7 (38.9, 40.6)	37.8 (37.3, 38.5)	36.0 (35.0, 36.9)	32.6 (31.7, 33.8)
<b>SNR<sub>Subvolume</sub> [dB]</b>				
Artery	6.8 (2.6, 8.7)	5.3 (2.1, 8.5)	11.8 (6.2, 15.4)	12.7 (10.0, 15.2)
RNFL	33.7 (32.4, 34.6)	32.2 (31.1, 33.4)	30.7 (29.7, 31.6)	28.7 (27.4, 29.6)
<b>Noise Level [RAW value]</b>	55,186 (51,028, 61,463)	110,620 (94,717, 124,661)	202,044 (179,693, 228,765)	146,278 (129,426, 165,785)
<b>SNR<sub>Subvolume</sub> / Peak SNR<sub>Subvolume</sub> [%]</b>				
Artery	4.68 (1.89, 7.09)	2.76 (1.32, 5.79)	1.40 (0.39, 3.27)	2.23 (1.19, 3.96)
RNFL	14.2 (10.7, 17.6)	17.3 (13.3, 22.3)	13.8 (10.9, 17.0)	13.9 (10.5, 17.0)
<b>SNR<sub>Subvolume</sub> / SNR<sub>B-scan</sub> [%]</b>				
Artery	0.05 (0.02, 0.07)	0.06 (0.03, 0.11)	0.38 (0.13, 0.73)	1.10 (0.58, 1.64)
RNFL	24 (16, 30)	27 (22, 34)	28 (24, 33)	42 (31, 48)

Results are presented as median (IQR)

571 RNFL: retinal nerve fibre layer, N: number of B-scans with matched vessel–RNFL annotations, SNR: signal-to-  
572 noise ratio, SNR<sub>B-scan</sub>: SNR in the complete B-scan, SNR<sub>Subvolume</sub>: SNR in the B-scan subvolume, RAW value:  
573 value extracted from the raw .vol OCT files, Peak SNR<sub>Subvolume</sub>: maximal SNR on a pixel level in the complete  
574 subvolume over time, IQR: interquartile range.

575 **Table 2.** Acquisition overview per nominal A-scan rate

	20 kHz, N = 109	40 kHz, N = 113	85 kHz, N = 122	125 kHz, N = 122
<b>B-scan Interval [ms]</b>	49 (49, 49)	25 (25, 25)	13 (13, 13)	9 (9, 9)
<b>Exam Duration [ms]</b>	4,224 (3,528, 5,317)	4,042 (3,582, 4,376)	3,411 (2,950, 3,759)	2,867 (2,059, 3,321)
<b>Annotated B-scans per Image Stack [n]</b>	86 (72, 108)	159 (141, 172)	253 (219, 279)	303 (218, 351)
<b>SNR<sub>B-scan</sub> [dB]</b>	39.8 (37.3, 42.4)	38.0 (35.3, 39.6)	34.6 (31.0, 36.0)	32.2 (29.9, 34.4)
<b>Peak B-scan Intensity [RAW value]</b>	555,997,151 (340,536,329, 1,034,710,323)	786,543,813 (345,832,675, 1,310,379,806)	685,001,499 (347,938,689, 963,279,206)	239,018,674 (168,368,268, 488,855,979)
<b>Annotated Image Stacks [N]</b>				
Optic nerve head centre	9 (8.3%)	13 (12%)	13 (11%)	13 (11%)
NRM	38 (35%)	31 (27%)	42 (34%)	42 (34%)
1 ODD from NRM	16 (15%)	17 (15%)	17 (14%)	17 (14%)
2 ODDs from NRM	14 (13%)	19 (17%)	17 (14%)	17 (14%)
3 ODDs from NRM	17 (16%)	17 (15%)	17 (14%)	17 (14%)
4 ODDs from NRM	12 (11%)	13 (12%)	13 (11%)	13 (11%)
5 ODDs from NRM	3 (2.8%)	3 (2.7%)	3 (2.5%)	3 (2.5%)

Results are presented as median (IQR) of the average values per image stack | N (% of image stacks per acquisition rate)

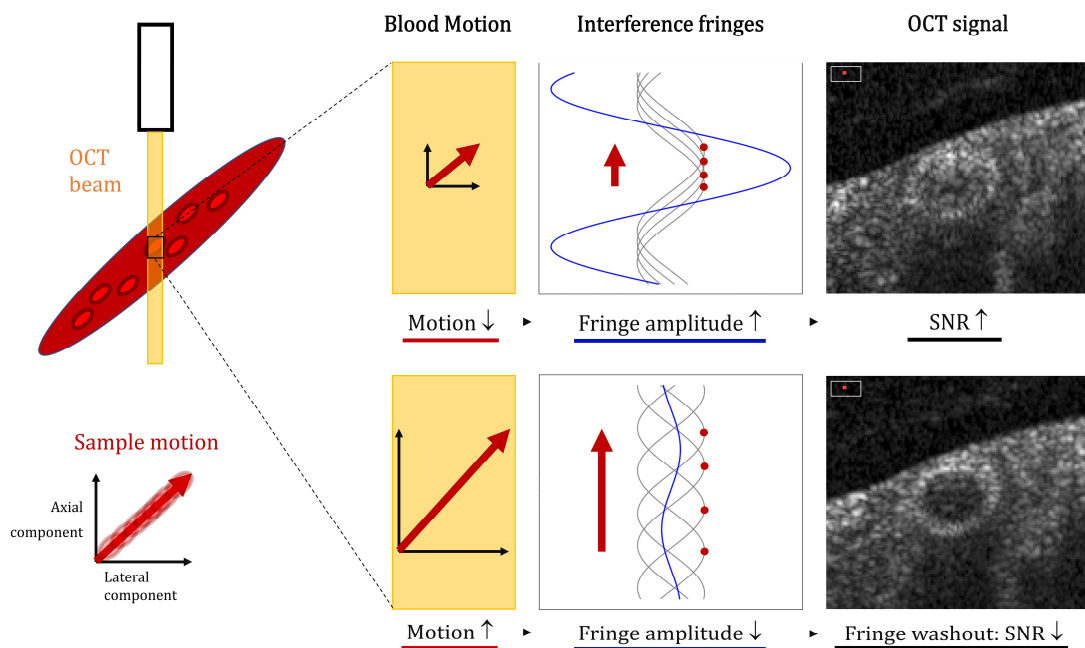
576 N: number of time-resolved image stacks, SNR<sub>B-scan</sub>: signal-to-noise ratio in the complete B-scan; RAW value:  
577 value extracted from the raw .vol OCT files; NRM: Neuroretinal rim, 1 ODD from NRM: eccentricity of 1 optic disc  
578 diameter from the neuroretinal rim, IQR: interquartile range.

**Table 3.** Vessel subvolume SNRs and calculated velocities

Variable	20 kHz, N = 109	40 kHz, N = 113	85 kHz, N = 122	125 kHz, N = 122
<b>SNR<sub>Vessel</sub> [unitless]</b>	400 (134, 995)	328 (151, 610)	159 (75, 312)	105 (50, 201)
<b>Vessel Intensity [RAW value]</b>	25,043,042 (7,035,096, 62,483,917)	42,599,201 (17,286,374, 73,869,286)	36,436,880 (16,508,790, 69,969,934)	15,610,795 (7,235,353, 30,854,052)
<b>SNR<sub>Vessel</sub> / Peak SNR<sub>Vessel</sub> [%]</b>	5.7 (4.6, 6.9)	5.4 (3.8, 6.9)	5.3 (3.8, 7.0)	5.0 (3.9, 6.6)
<b>Average Velocity [a.u.]</b>	7 (6, 8)	14 (12, 16)	29 (26, 33)	43 (38, 48)
<b>Minimal Velocity [a.u.]</b>	5 (5, 5)	11 (10, 11)	22 (22, 23)	33 (32, 34)
<b>Maximal Velocity [a.u.]</b>	8 (7, 10)	17 (14, 21)	35 (29, 44)	53 (43, 62)

Results are presented as median (IQR) of the average values per image stack

N: number of time-resolved image stacks, SNR: signal-to-noise ratio, SNR<sub>Vessel</sub>: Average SNR in the vessel subvolumes of the B-Scan, RAW value: value extracted from the raw .vol OCT files, Peak SNR<sub>Vessel</sub>: maximal SNR on a pixel level in the complete vessel subvolume over time, Average Velocity: average of the numerical solutions to the SNR<sub>Drop</sub> equation per B-scan, Minimal Velocity: smallest numerical solution, Maximal Velocity: largest numerical solution, a.u.: arbitrary unit, IQR: interquartile range.



587

588 **Figure 1.** Illustration of the fringe washout in spectral-domain optical coherence tomography (OCT). Fringe  
589 washout describes the signal drop in the OCT when the sample moves through the sample beam during  
590 illumination. The sample motion can be split into two components: a lateral component and an axial component.  
591 When the integration time is shorter or the velocity is smaller, there is less motion, the fringe amplitude is higher  
592 and, hence, the OCT intensity is higher. When the integration time is longer or the velocity is higher, the sample  
593 has a larger motion, which leads to a lower fringe amplitude. This fringe washout causes a higher SNR drop and  
594 a lower OCT intensity (bottom right).

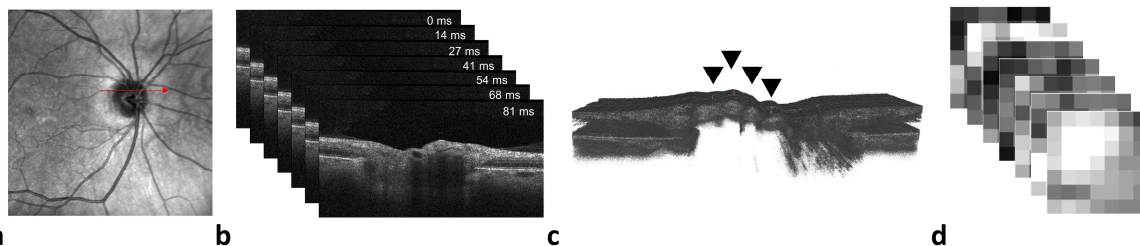


**Figure 2.** Time-resolved dynamic optical coherence tomography-based extraction of vessel subvolumes. **a** Scanning laser ophthalmoscopy (SLO) image. The red arrow indicates the position of the continuous acquisitions, which can be started by a press on the joystick. **b** The time-resolved B-scans are continuously acquired with a time stamp for each B-scan. **c** The continuous images are registered and reconstructed as a three-dimensional volume, where the third dimension represents the time axis. On each B-scan, the vessel centres were manually annotated. **d** Subvolumes of  $7 \times 7$  pixels surrounding the vessel centre were extracted and further processed for fringe washout analysis.

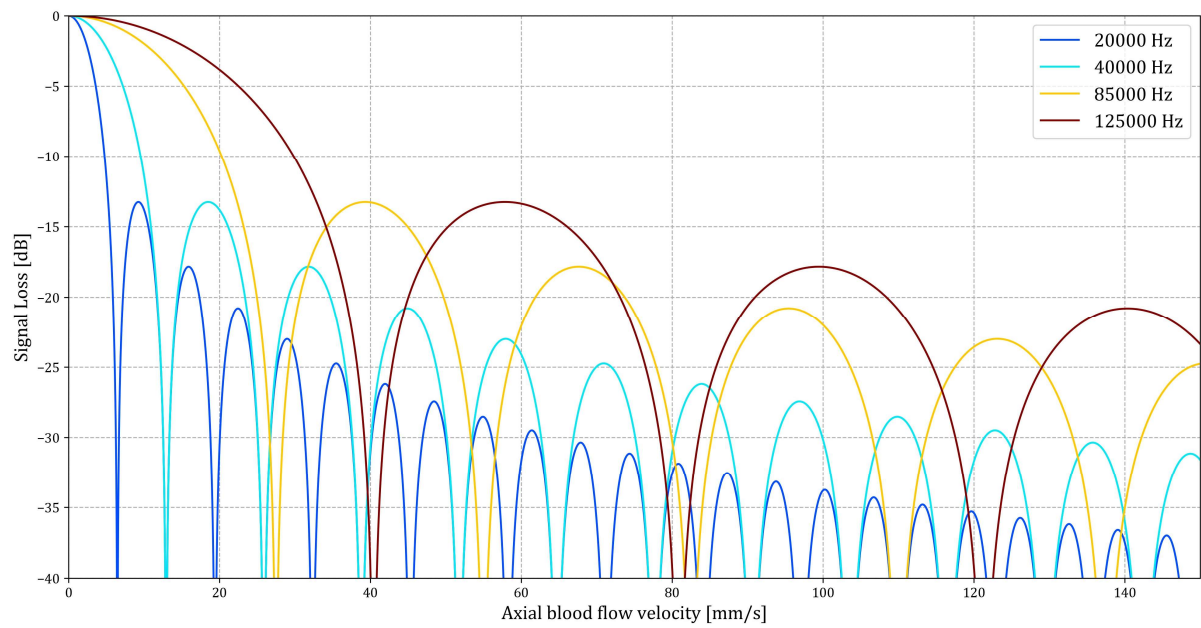
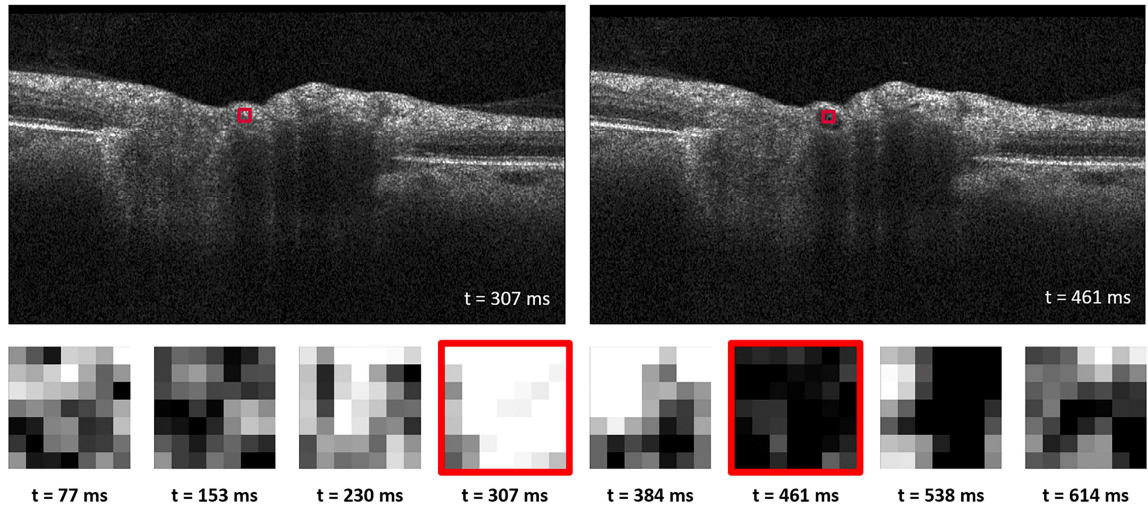
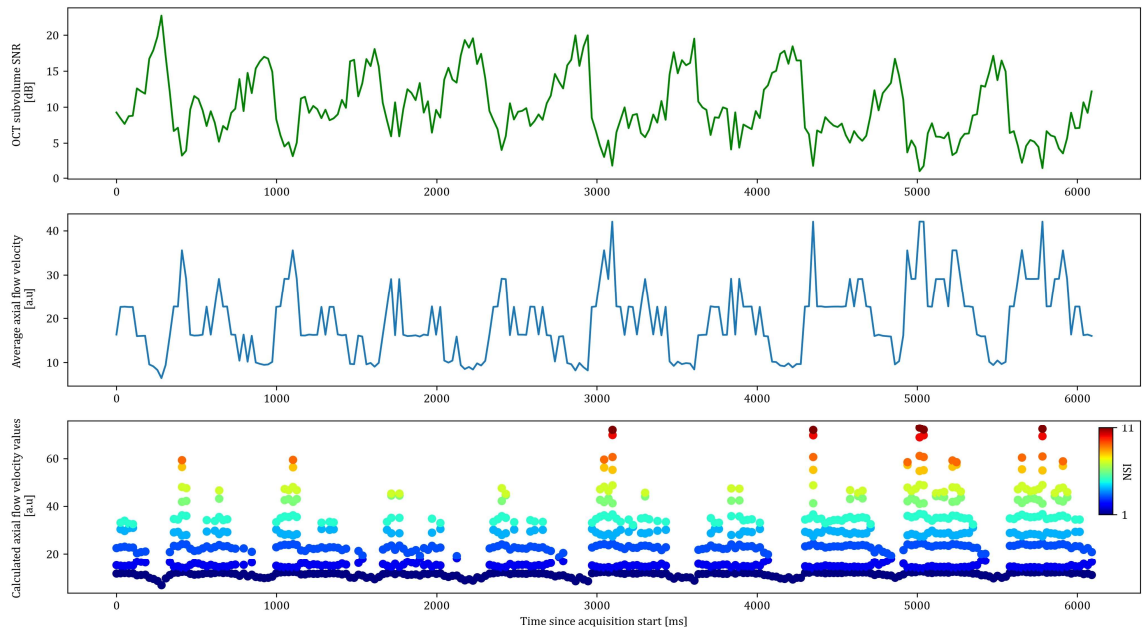


**Figure 3.** Axial blood flow velocity component calculation. The axial blood flow velocity is calculated at SNR drops for the four nominal acquisition rates of 20, 40, 85 and 125 kHz. As seen, several potential axial blood flow velocities are based on a single signal-to-noise ratio (SNR) drop. The numerical solutions to the equation were used to generate the blood flow profiles in the time-resolved dynamic OCT acquisitions. The values here represent the calculated velocities in mm/s, where the SNR drop is compared against a known reference SNR.



**a**



**b**

**Figure 4.** Time-resolved optical coherence tomography (OCT) B-scans of optic nerve head vessels. **a** Imaging was performed at the same location. Two B-scans and eight extracted  $7 \times 7$  pixel arterial subvolumes ( $20 \times 27 \mu\text{m}$ ) are shown with timestamps. The corresponding subvolumes are framed in red, where the red frame on the original B-scan is enlarged for better visualisation. The intensity changes in the subvolume occur due to varying fringe washout of the arterial signal over time. **b** Analysis of retinal blood flow dynamics over 6 s in an artery with time-resolved OCT (A-scan integration time of  $22.4 \mu\text{s}$ , inter-B-scan interval of  $\sim 25$  ms). Timestamp-matched mean SNR of the OCT subvolume (top row), average axial flow velocity (middle row) and calculated axial flow velocity values (bottom row) are presented. The average axial flow velocity line (middle row) represents the average of the numerical solutions, and the dots (bottom row) represent all numerical solutions to the  $\text{SNR}_{\text{Drop}}$  equation. dB: decibel, a.u.: arbitrary unit, NSI: numerical solution index.

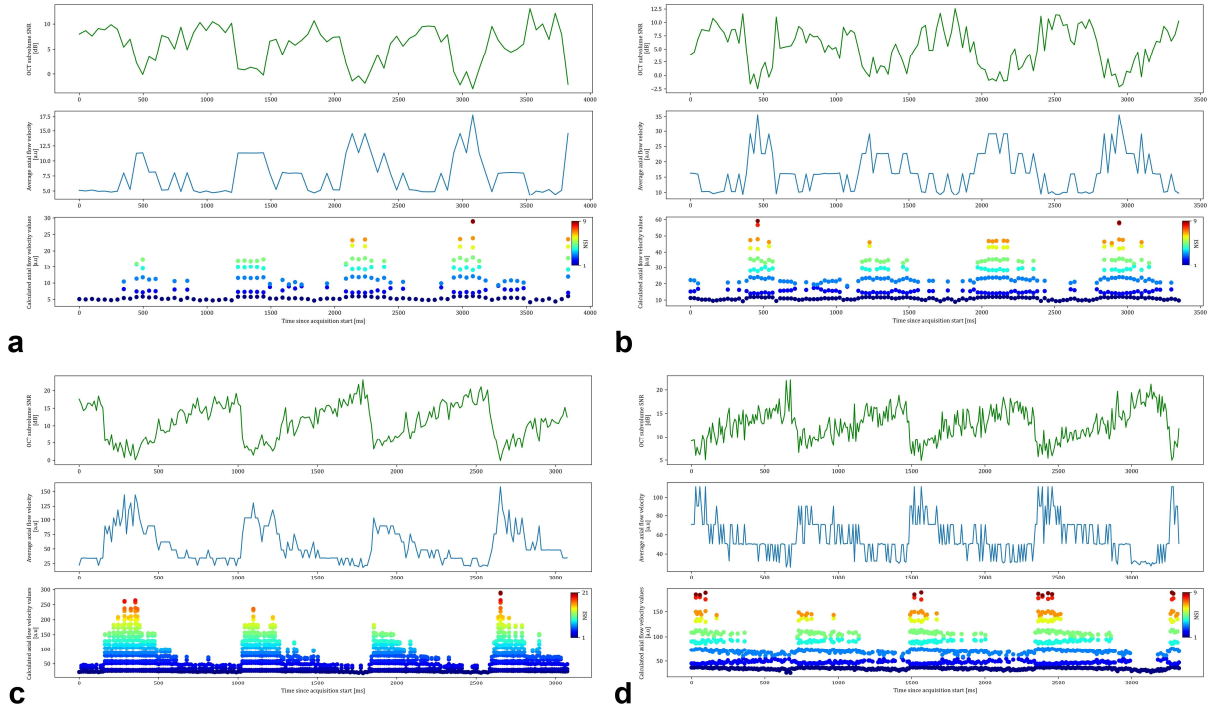


**Figure 5.** Calculated flow velocity profiles of time-resolved OCT intensity at the four different nominal acquisition rates (**a** 20 kHz, **b** 40 kHz, **c** 85 kHz and **d** 125 kHz). Each subfigure shows the acquisition duration in ms from the start on the x-axis. On the y-axes, the mean OCT SNR from the subvolume can be found on the top row, the average flow velocity (average of the numerical solutions to the  $SNR_{Drop}$  equation) in blue on the middle row and the calculated flow profiles (all numerical solutions) as dots on the bottom row.

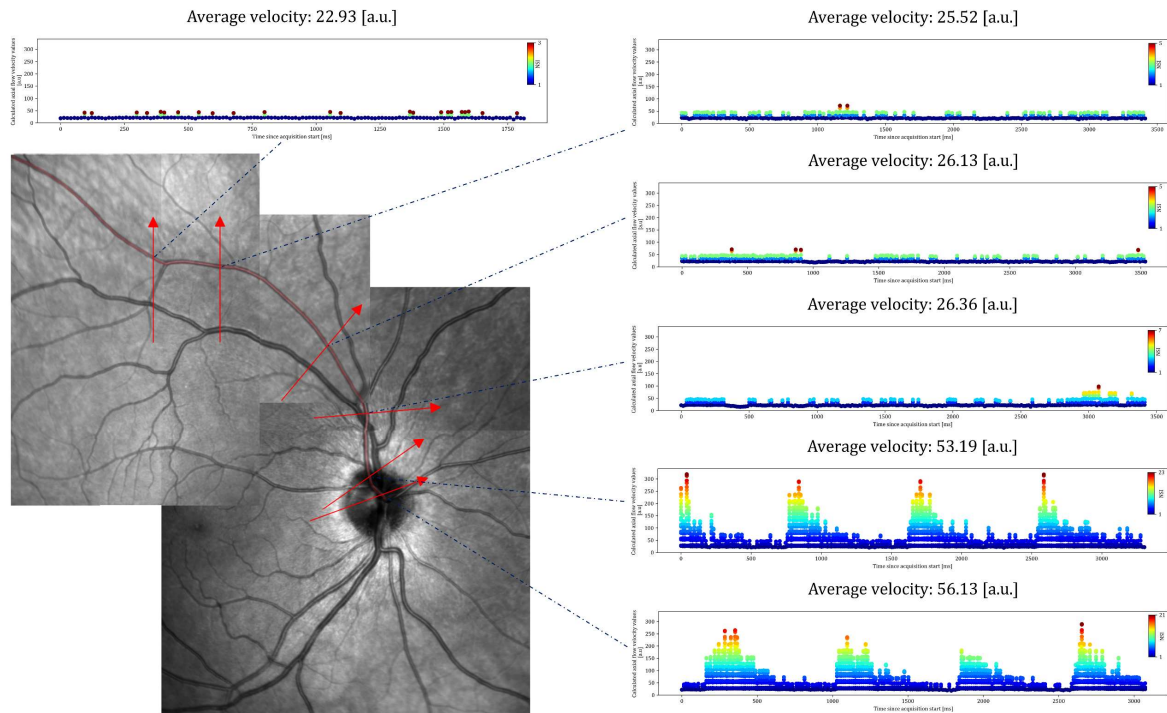
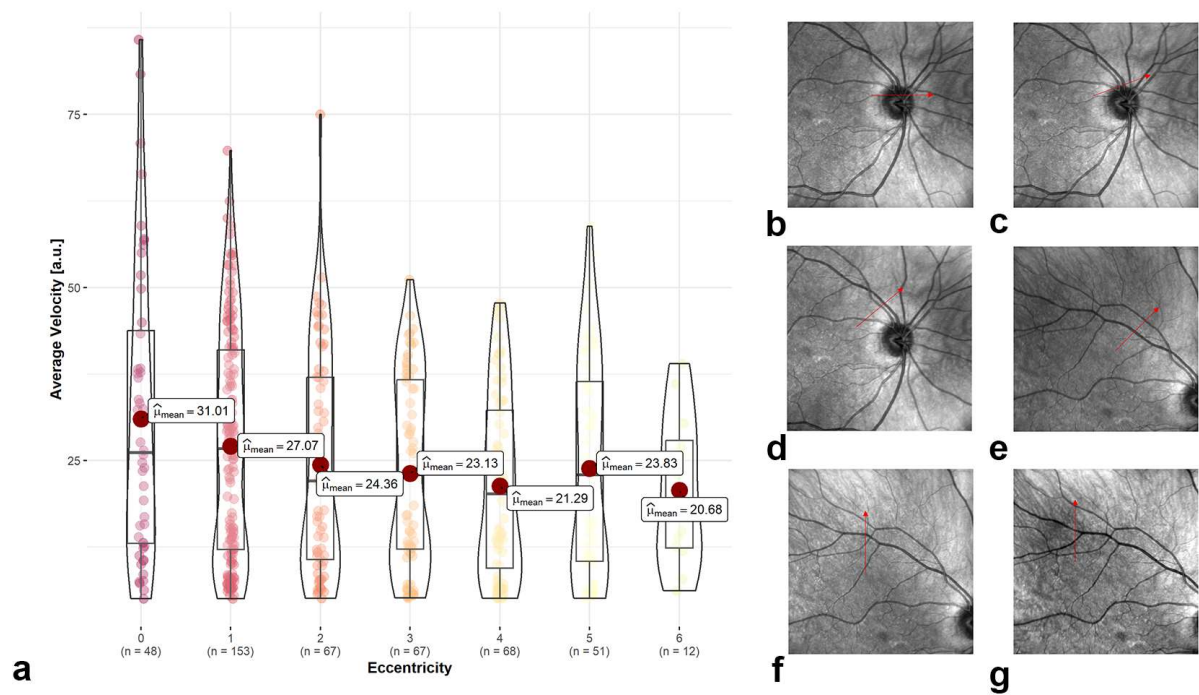


**Figure 6.** En-face representation of time-resolved acquisitions along an artery. The montage scanning laser ophthalmoscopy (SLO) of different acquisitions in the bottom left indicates the OCT acquisition locations as arrows, and the analysed artery is presented in transparent red. The corresponding time-resolved dynamic blood flow profiles show a clear pulsatility close to the optic nerve head centre, which diminishes beyond the optic nerve head rim. The estimated average blood flow velocities decrease from the optic nerve head centre towards the periphery.



634

635 **Figure 7. a** Estimated average blood flow velocity of the measured vessels at different eccentricities represented  
636 as violin-boxplots and with the means highlighted as red dots. **b–g** Example scanning laser ophthalmoscopy  
637 (SLO) acquisitions with the positioning of the continuous B-scans highlighted by a red arrow corresponding to  
638 eccentricities 0–5. **b**  $\triangleq$  0: Optic nerve head centre, **c**  $\triangleq$  1: Neuroretinal rim, **d**  $\triangleq$  2: eccentricity of 1 optic disc  
639 diameter (ODD) from the neuroretinal rim, **e**  $\triangleq$  3: eccentricity of 2 ODDs from the neuroretinal rim, **f**  $\triangleq$  4:  
640 eccentricity of 3 ODDs from the neuroretinal rim, **g**  $\triangleq$  5: eccentricity of 4 ODDs from the neuroretinal rim.

641 **Supplementary Material**

642 **Supplementary Video 1**

643 Time-resolved dynamic optical coherence tomography of an artery (cross-sectional)  
644 at the centre of the optic nerve head.

645

646 **Supplementary Video 2**

647 Time-resolved dynamic optical coherence tomography of an artery (longitudinal) at  
648 the centre of the optic nerve head.

649

650 **Supplementary Video 3**

651 Comparison of time-resolved dynamic optical coherence tomography with  
652 corresponding blood flow velocity profiles at four different integration times.